Data preparation for prestack depth migration

Hugh D. Geiger

SUMMARY

The goal of prestack depth migration is to reconstruct an image of the subsurface with the highest possible resolution. Given that seismic data is bandlimited, the ideal response from the complete sequence of data preprocessing and imaging is an image where each reflector is represented as zero-phase bandlimited singular functions with the peak positioned at the reflector and the peak amplitude proportional to the angle-dependant reflection coefficient. To achieve this goal, each step of the sequence needs to be understood and implemented correctly. This is a challenge even with the simplest constant-velocity synthetic data. Key considerations include: 1) preprocessing of the data to a zero phase wavelet, 2) accurate modelling of the source signature as a zero-phase wavelet, and 3) phase and amplitude stability of the extrapolators. 2-D synthetic models are used to show how uncorrected static shifts and non-zero-phase wavelets affect the resolution of the image.

INTRODUCTION

The three most common imaging conditions for multidimensional prestack seismic imaging are based on the principles of excitation time, cross-correlation, and deconvolution (Claerbout, 1971). These imaging conditions are applied in the time-domain to either a single extrapolated trace or a pair of extrapolated traces, yielding a value representing bandlimited reflectivity at the extrapolation depth. The 1-D deconvolution imaging condition can be shown to be an essential part of the formulation of relative-amplitude-preserving Kirchhoff and diffraction stack migration methods (Docherty 1991; Hanitszch 1997; Dellinger et al. 2000, Bleistein et al. 2001), and suitable for relative-amplitude-preserving prestack wave-equation shot-profile migration (de Bruin et al. 1990). The 1D excitation imaging condition is commonly used in reverse-time migration (Zhu and Lines 1998), and can be shown to be approximately correct for both relative-amplitude-preserving diffraction stack and wave-equation shot-profile migrations when the shot records have been preprocessed with gain correction (Al-Saleh and Geiger, 2004 – this report). Recently, a variety of multidimensional imaging conditions have been proposed, either for improved spatial resolution (Valenciano and Biondi, 2003), or for the extraction of amplitude-versus-angle response using wave-equation survey-sinking migration (e.g. Kuehl and Sacchi 2003; Sava and Fomel 2003). For all these methods, basic concepts of optimal 1-D resolution of wavelets in the time domain can be extended to resolution in the depth image.

In the depth image, Bleistein et al. (2001) choose a bandlimited singular function to quantify the ideal reflector, and then design their Kirchhoff-Born inversion schemes to image these functions. Along any line normal to the reflector, a bandlimited singular function can be thought of as a bandlimited delta function, although for practical purposes, any bandlimited zero-phase wavelet will suffice. I will use a Ricker wavelet (Ricker 1953). These are appropriate functions because they are spatially compact (i.e. they have a limited extent normal to the reflector,) and because their peak amplitude is

centered on the discontinuity in elastic properties represented by the reflector. Thus, many of the concepts of 1D resolution formulated for seismic time sections (see Brown 1999; Yilmaz 2001) can be applied to depth sections. In this study, I look at two important characteristics of bandlimited zero-phase wavelets - dominant frequency and bandwidth – and investigate wavelets as they pass through the filters defined by 1-D imaging conditions. In addition, I use the 2-D Marmousi acoustic data set (Versteeg and Grau 1991) to examine source modelling, and to illustrate effects of phase rotation and static shifts on the accuracy of reflector imaging.

WAVELET PROPERTIES FOR 1D RESOLUTION

For 1-D resolution, the zero-phase wavelet has two important properties: dominant frequency and bandwidth (Brown, 1999). The ominant frequency is related to peak-width resolution. The width of the wavelet peak from zero-crossing to zero-crossing can be defined approximately equal to $T/2$ or $1/(2*f_{dom})$, where T is the period of f_{dom} - the dominant frequency of the wavelet - and f_{dom} is approximately equal to the median frequency.

The bandwidth of the zero-phase wavelet is related to peak-height resolution. The ratio of trough-height to peak-height is approximately equal to $1/B$, where B is the bandwidth in octaves. A wavelet with a larger bandwidth will have correspondingly smaller sidelobes. However, large bandwidth does not necessarily yield a compact wavelet. Yilmaz (2001) points out that steep slopes in the wavelet's amplitude spectrum can result in a wavelet with a ringy appearance.

The two zero-phase wavelet properties of dominant frequency and bandwidth are important in the design of imaging conditions. Ideally, we would like our output depth section to have the depth-equivalent properties of high dominant frequency and large bandwidth. A bandlimited singular function with small peak width is important for defining reflector structure and resolving thin beds, while small sidelobes help reduce the interference between nearby reflectors. Limited interferernce is important, given that most relative-amplitude preserving migrations extract peak amplitude as a measure of reflectivity. High dominant frequency and large bandwidth are also desirable properties for a modeled source wavelet, and as an appropriate goal for the embedded wavelet after preprocessing of the shot record. Care must be exercised, however, because both the cross-correlation and deconvolution imaging conditions combine the source and embedded wavelets, with the potential for producing a less desirable imaging wavelet.

In Figure 1, the dominant frequency is progressively increased from 15-20-25-30 Hz, while the bandwidth is kept relatively constant at 2-2.2 octaves. Notice how the peak width of the Ricker wavelet narrows, but the ratio of the trough height to peak height remains relatively constant. In Figure 2, the dominant frequency of the wavelets in Figure 1 has been doubled to 30-40-50-69 Hz, while keeping the bandwidth relatively constant at 2-2.2 octaves. This has effectively doubled the peak width resolution, with no change in the ratio of peak trough to peak height. In Figure 3, the 30 Hz Ricker wavelet from Figures 1 and 2 has been whitened using a trapezoidal filter in the frequency domain to yield a [1 3 48 62.5] Hz amplitude spectrum. The dominant frequency is approximately
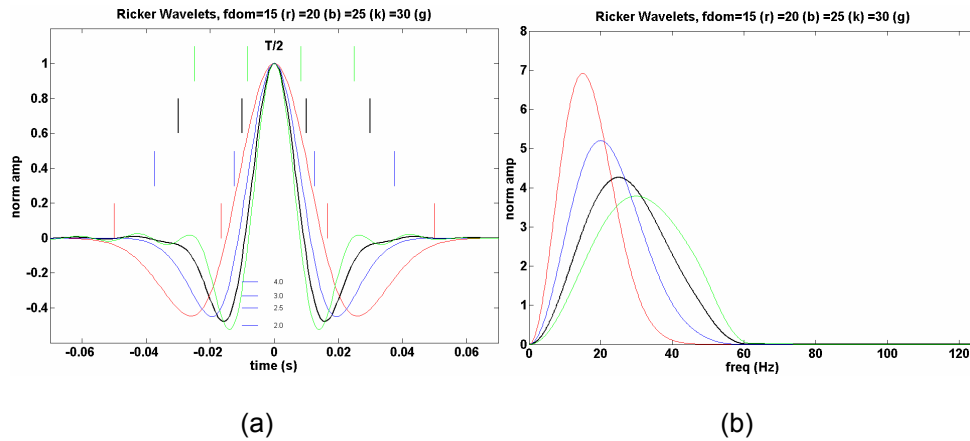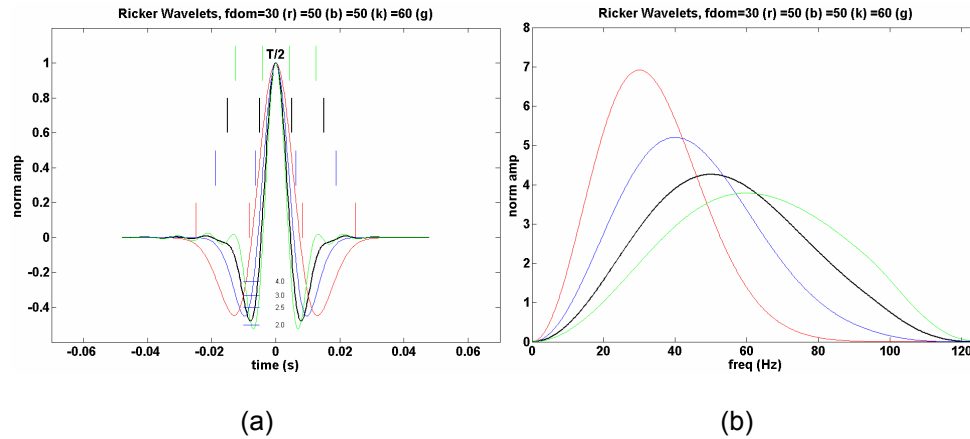
(a)　　　　　　　　　　　　　　　(b)

FIG. 1. Four Ricker wavelets with a different dominant frequency fdom = 15, 20, 25, 30 Hz but similar bandwidth B = 2-2.2 octaves. Notice how the peak width [~ T/2 or ~1/(2*fdom)] decreases with increasing fdom, but the ratio of the peak trough to peak height (~1/B) remains constant.

(a)　　　　　　　　　　　　　　　(b)

FIG. 2. Four Ricker wavelets with a different dominant frequency fdom = 30,40,50,60 Hz but similar bandwidth B = 2-2.2 octaves. Compared to Figure 1, the peak width resolution has effectively doubled by doubling the dominant frequency, with no increase in bandwidth. The ratio of the peak trough to peak height remains relatively constant.
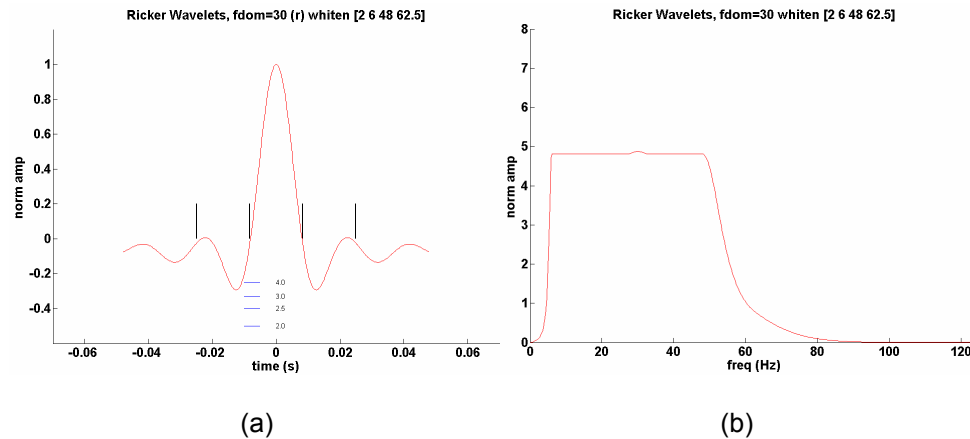

(a)　　　　　　　　　　　　　　　(b)

FIG. 3. A 30 Hz Ricker wavelet whitened to [2 6 48 62.5] Hz. After whitening, the dominant frequency is the same as the 30 Hz wavelets in Figures 1 and 2..The effective bandwidth has been increased by half from ~2-2.2 to ~3.7 octaves, which reduce the peak trough to peak height ratio by a 1/3.

the same, so there is no change in peak width. The bandwidth has increased by one-half from approximately 2-2.2 to 3.5, yielding a one-third reduction in peak trough to peak height ratio. A wavelet similar to Figure 3 is a reasonable goal for whitening, and a desirable singular function in the space domain of the image.

Notice that the wavelet in Figure 3 is no longer compact. The steeper slopes in the amplitude spectrum produce some ringing. In this case, the frequency boosting at the low end would be almost impossible to achieve in practice, but some additional shaping might be possible at the high end. With most conventional seismic data, bandwidths of between 2.5-3.5 octaves are achievable given favorable acquisition conditions and good pre-processing (Brown 1999).

IMAGING CONDITIONS

Assume that, with favourable acquisition and processing, we obtain a wavelet within the range of those displayed in Figures 1-3. In addition, assume that, if required, we are able to model the forward propagating shot impulse as a propogating zero-phase wavelet with a spectrum similar to those displayed in Figures 1-3. What kind of image will we get out if we apply one of the three basic imaging conditions: excitation time, cross-correlation, or deconvolution?

The excitation time imaging condition is the easiest to analyze. In fact, in the ideal case, it can be predicted as a velocity-stretched copy of the embedded wavelet contained in the backward extrapolated shot-record.

The cross-correlation imaging condition will combine the modeled source and embedded shot-record wavelets. Given the Fourier transform $U(\mathbf{x}_G, \omega; \mathbf{x}_s)$ of a trace in the backward-extrapolated upward-travelling shot-record wavefield U at depth point $\mathbf{x}_G$ for the source at $\mathbf{x}_s$, and the Fourier transform $D(\mathbf{x}_G, \omega; \mathbf{x}_s)$ of a trace in the forward-extrapolated downward-travelling modeled shot wavefield D at the same depth point $\mathbf{x}_G$ and for the same source $\mathbf{x}_s$, the reflectivity $R(\mathbf{x}_G; \mathbf{x}_s)$ is the zero lag of the cross-correlation imaging condition given by

$$R(\mathbf{x}_G; \mathbf{x}_s) = \sum_\omega \mathrm{Re}\left(U(\mathbf{x}_G, \omega; \mathbf{x}_s) D^*(\mathbf{x}_G, \omega; \mathbf{x}_s) \right). \tag{1}$$

An additional summation can be made over shot images at $\mathbf{x}_s$ to create a stacked image.

The deconvolution imaging condition also combines the modeled source and embedded shot-record wavelets. Using the same variables as in Equation (1), the deconvolution imaging condition can be thought of as the zero-lag of a normalized cross-correlation with stabilization factor $\varepsilon^2(\mathbf{x}_G, \mathbf{x}_s)$:

$$R(\mathbf{x}_G; \mathbf{x}_s) = \sum_\omega \frac{\mathrm{Re}\left(U(\mathbf{x}_G, \omega; \mathbf{x}_s) D^*(\mathbf{x}_G, \omega; \mathbf{x}_s) \right)}{D(\mathbf{x}_G, \omega; \mathbf{x}_s) D^*(\mathbf{x}_G, \omega; \mathbf{x}_s) + \varepsilon^2(\mathbf{x}_G, \mathbf{x}_s)}. \tag{2}$$

Valenciano and Biondi (2003) suggest that the best choice for $\varepsilon^2\left(\mathbf{x}_G, \mathbf{x}_s\right)$ depends on the spatial location of both the image point and the source. They propose that a reasonable estimate for $\varepsilon^2\left(\mathbf{x}_G, \mathbf{x}_s\right)$ can be determined as a scaled mean (over frequency) of the downward propagating shot trace:

$$\varepsilon^2\left(\mathbf{x}_G, \mathbf{x}_s\right) = \lambda \left\langle D\left(\mathbf{x}_G, \omega; \mathbf{x}_s\right) D^*\left(\mathbf{x}_G, \omega; \mathbf{x}_s\right) \right\rangle . \qquad (3)$$

Kelly and Ren (2003) also suggest a spatially variable stabilization factor. They present both iterative and least squares approaches as modifications to the method of Valenciano and Biondi (2003), and conclude that both methods can produce excellent images - far superior to methods using an arbitrary constant or 'guesstimate' value for $\varepsilon^2\left(\mathbf{x}_G, \mathbf{x}_s\right)$. I am currently developing a spatial- and shot-variable stabilization factor with thresholding that tapers and removes portions of the image poorly illuminated by the shot. The Marmousi image shown in Figure 12 is produced using this method. More details are forthcoming.

SOURCE MODELLING

The wavelet in the modeled shot can be designed to yield a zero-phase propagating wavelet with the peak amplitude marking the time elapsed since source initiation. However, directional variations can arise both from the source array and from ghost effects. As well, the unknown true propagating source wavelet will experience phase and amplitude variations due to the Earth filter (for example, attenuation and thin-bed multiples – similar variations are present in most finite difference synthetic data). These wavelet variations are not properly accounted for when using one-way scalar wavefield extrapolators, so there is no guarantee that the source wavelet will arrive at the reflector location as an optimal zero-phase wavelet.

One-way scalar wavefield extrapolators introduce another issue worth addressing. It is well known that the wavefield from an input monopole source function propagates as a dipole response (Wapenaar 1998). The exact response function depends on the dimensionality of the extrapolator (2-D, 2.5-D, or 3-D). A simple way around this problem is to seed the source function at a desired depth (e.g. 25 m for Marmousi) using analytic Green's functions. One advantage of this approach is that source arrays and ghosted sources can be easily modeled, even if the spacing within the array does not match the grid spacing chosen for wavefield extrapolation. Simple constant velocity Green's functions can be used in marine or land situations where the near surface velocity is constant. Kelly and Ren (2003) propose a clever extension to this method for modelling land sources in areas of complex velocity structure. A constant velocity appropriate for the immediate region around the source array is used to fill the half-space below the source. The source array and any ghosting effects are modeled at shallow depth using constant-velocity analytic Green's functions. The analytic wavefield is then backward extrapolated to the surface. The resulting wavefield should be localized in the vicinity of the original source and can now be used as input for extrapolation through a model of any complexity, including models with strong near-surface lateral and vertical velocity variations typically encountered in land surveys.

Modelling an accurate source wavelet with correct relative amplitude is essential for relative-amplitude preserving migration (Dellinger et al. 2000; Kelly and Ren 2003). An example of a modeled source wavelet for the 2-D Marmousi synthetic data set is shown in Figure 4. The source array was modeled using analytic 2-D Green's functions representing 6 water guns at 8m spacing and a depth of 8m, and 6 ghosts as mirror sources of opposite sign. The wavelet has been rotated to zero phase, which corrects for the half-integral filter of the 2-D Green's function and the full derivative filter of the dipole effect of the ghost (see e.g. Geiger 2001; Deregowski and Brown 1983). The source array, combined with the dipole of the ghost, creates a directed array where higher angles of propagation are significantly attenuated. The wavelet after whitening is shown in Figure 5. The whitening parameters produce only a moderate amount of ringing.
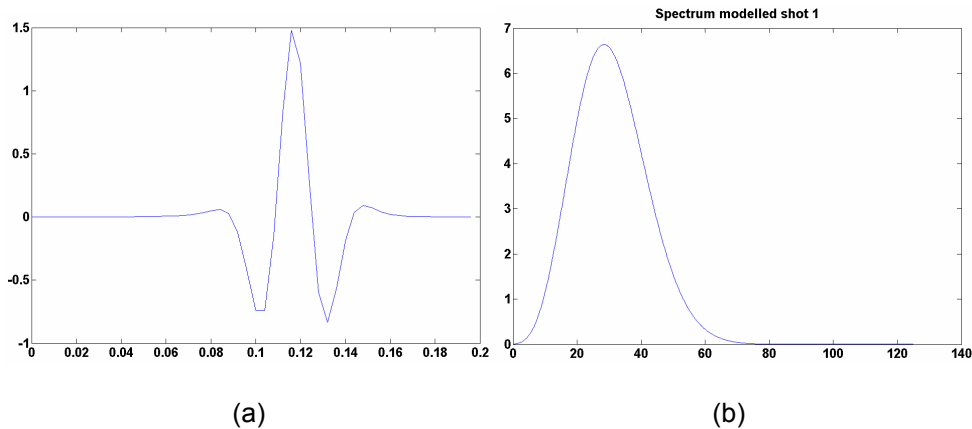

(a)   (b)

FIG. 4. a) Marmousi source impulse modeled at 24m depth. b) Amplitude spectrum of the source with a dominant frequency fdom = 25 Hz, and bandwidth B ~ 2 octaves. The source array was modeled using analytic 2-D Green's functions representing 6 water guns at 8m spacing at a depth of 8m, and 6 ghosts as mirror sources of opposite sign. The wavelet has been rotated to zero phase, correcting for the half-integral filter of the 2-D Green's function and the full derivative filter of the dipole effect of the ghost.
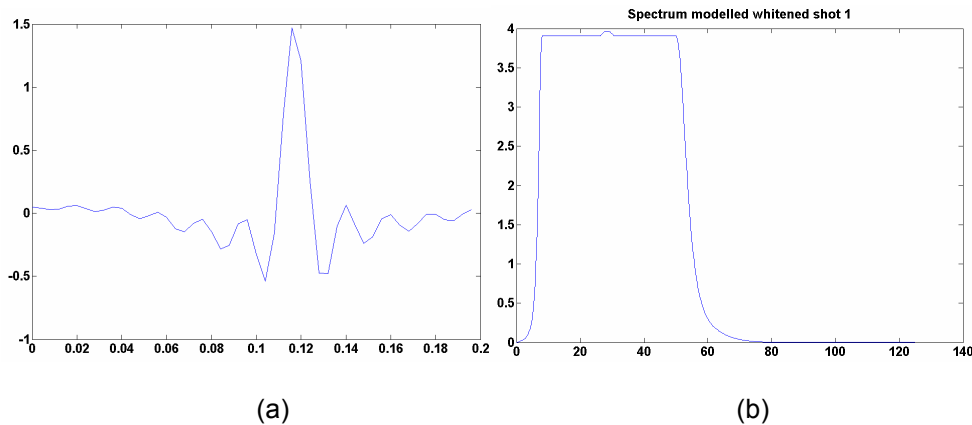

(a)   (b)

FIG. 5. a) Marmousi source impulse from Figure 4 after whitening to [4 8 55 80]. b) Amplitude spectrum with fdom = 25 Hz and bandwidth B ~ 3 octaves.

The original Marmousi shot records were produced using a relatively coarse 4m finite difference grid. This created some high frequency dispersion noise that was removed by a [0, 10, 35, 55] bandpass filter at the time the data were generated (Verstee and Grau 1991). The applied filter effectively limits the amount of whitening that can be applied to either the low end or the high end. The dispersion effects will be most pronounced at long-range low-velocity propagation, where they will appear (to first order) as a significant static shift or phase rotation of the wavelet. However, these wavelets will be recorded along with wavelets from deeper reflectors where the propagation path is predominantly at a much higher velocity and dispersion is minimal. This problem might best be tackled by regenerating the Marmousi dataset using more advanced finite difference techniques.

STATIC SHIFTS AND PHASE ROTATION

A good depth image contains well-focused reflectors that are accurately positioned in space. Focusing and positioning are compromised if either the modeled shot or the shot record contain uncorrected static shifts or phase rotations relative to the other. A simple explanation is as follows. The central peak of the bandlimited reflector image is created when the wavelet in the forward extrapolated source record and the reflection event in the backward extrapolated shot-record are time coincident. With an uncorrected relative static shift between the two, time coincidence will occur at a different extrapolation depth (and different lateral position for wavefields propagating non-vertically). In this case, both wavefields will be either under- or over-extrapolated, and the resulting image will not be optimally focused. Uncorrected relative phase rotations will produce similar effects but of smaller magnitude. Note that the extrapolation operators are independent of time. Hence, if both wavefields have identical static shifts or phase rotations, an image with good focusing and accurate positioning can still be obtained.

Phase rotations and static shifts in shot records are difficult to identify because we don't know the shape of the embedded wavelet. In all likelihood, the embedded wavelet is mixed phase. A deconvolution operator that creates a zero-phase wavelet will probably introduce (or leave as uncorrected) some unknown component of static shift. In addition, a zero-phase embedded wavelet may not be the ideal response. Thus, the problem can persist even after what might be considered ideal processing.

A simple acoustic finite-difference model can be used to determine approximate static shifts and phase rotations suitable for correcting shot records. The finite-difference model is designed to isolate the wavefield response from a single subsurface reflector, while incorporating some of the key near-surface effects such as arrays, ghosting, and velocity contrasts that might generate short period multiples (e.g. shallow water bottom multiples). The input source wavelet and both the source and receiver arrays should match the actual acquisition parameters as closely as possible. If the data are synthetic (as is the case with Marmousi), the test program should duplicate key parameters such as grid spacing and the order of the finite difference operators. The resulting finite difference traces can then be used to test and compare pre-processing options such as deconvolution and whitening. The goal is to create a zero-phase wavelet with dominant frequency and bandwidth characteristics as described earlier in this paper (e.g. Figure 3). An appropriate static shift can be determined by comparing the observed traveltime at the

peak of the processed zero-phase wavelet against an exact traveltime of the reflection event computed analytically or by raytracing. We used this approach to model the near surface effects of the Marmousi model (Geiger and Daley 2003). A good zero-phase wavelet was produced using a simple predictive decon (200ms operator length, 52 ms gap, and .0002 stability factor), combined with zero-phase whitening and a –60ms static shift. This processing was applied to the Marmousi shot records prior to imaging. Note that the parameters chosen for the predictive decon are quite gentle. Youn and Zhou (2001) propose a mute function combined with a more aggressive predictive decon (160ms operator, 12 ms gap, stability factor unknown). It is quite possible that a better image might be created given more testing of processing parameters.

The Marmousi data set is ideal for illustrating the effect of an uncorrected static shift in the shot record. Figure 6 is the Marmousi velocity model, with a red box highlighting the area imaged in Figures 7-10. Figure 7 is the bandlimited reflectivity, with a black sawtooth line marking the position of a reference reflector for Figures 8-10.
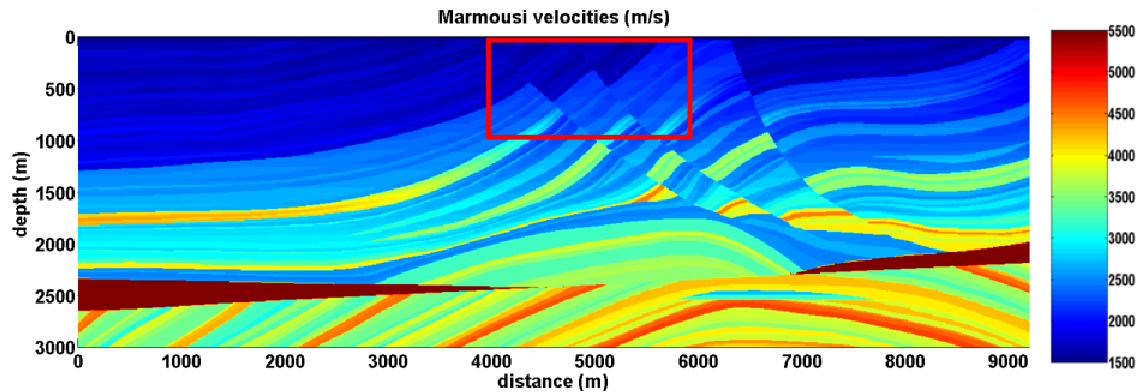

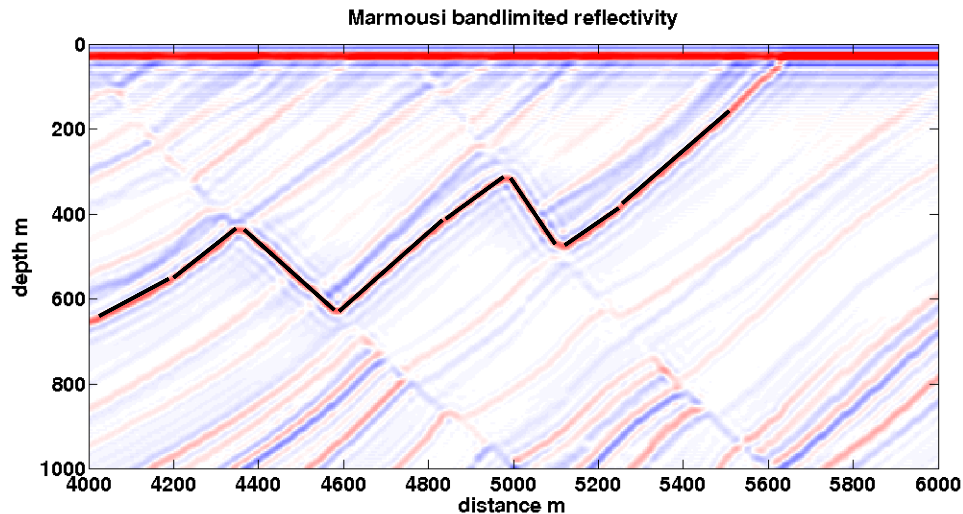FIG. 6. Marmousi velocity model. The area outlined in red is imaged in Figures 7-12.

FIG. 7. Marmousi bandlimited reflectivity. The black sawtooth line marks a reference reflector for Figures 8-10.
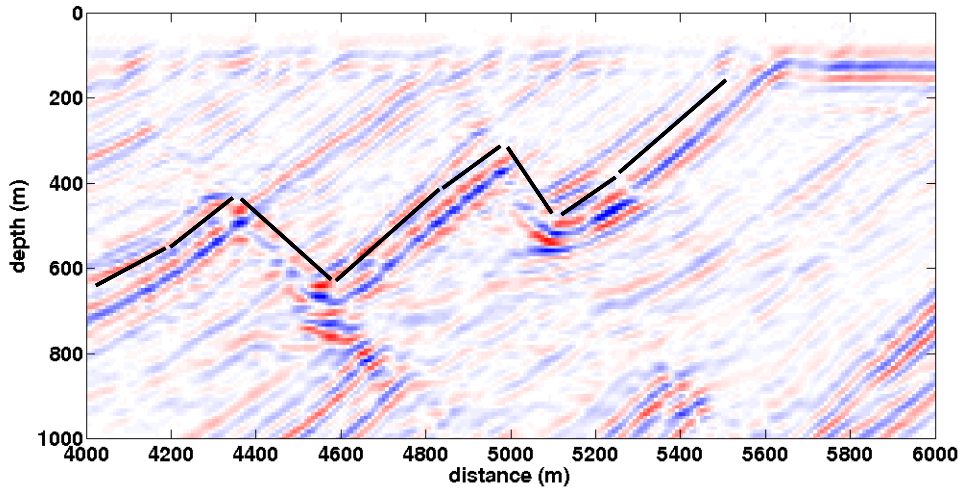
FIG. 8. Marmousi data; gap decon; whitened; 0ms static; PSPI cross-correlation imaging.
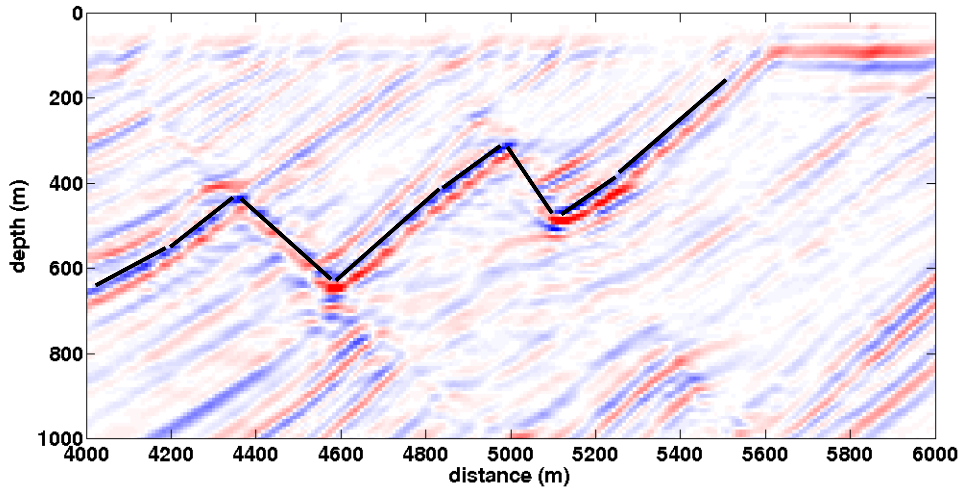

FIG. 9. Marmousi data; gap decon; whitened; -32ms static; PSPI cross-correlation imaging.
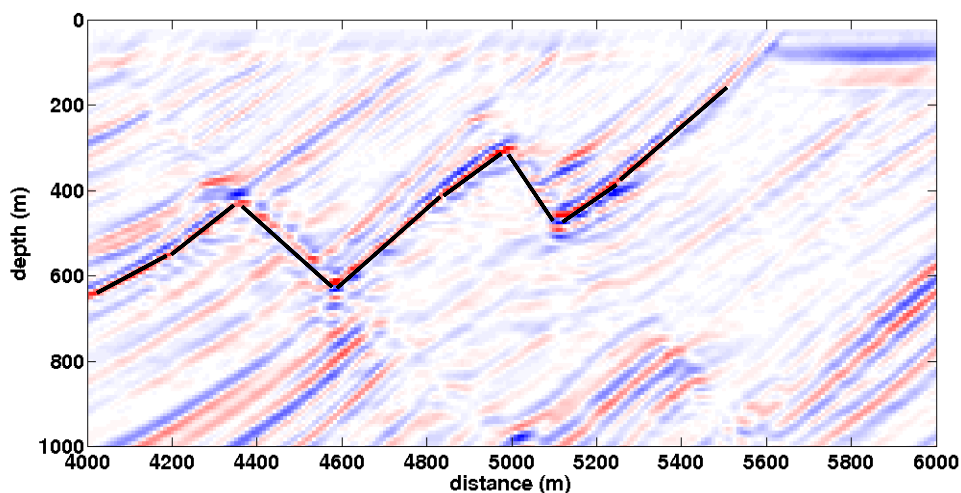
FIG. 10. Marmousi data; gap decon; whitened; -60 ms static; PSPI cross-correlation imaging.

The images in Figures 8-10 are processed and migrated using identical parameters, with the exception of the static shift applied to the input data after predictive deconvolution and whitening, but prior to migration. Figure 8 is the image from the data with no static applied; Figure 9 with a –32ms static (data advanced in time), and Figure 10 with a –60 ms static. The -60ms static is the static suggested by the finite difference modelling and processing exercise described earlier, and appears to be very close to optimal. Each of the images was produced by an unweighted stack of depth images from 87 shot records migrated using phase-shift plus interpolation (PSPI, Gazdag and , with source locations every 25 m from 4000 m to 6175 m in x. The individual depth images were created using a simple cross-correlation imaging condition (equation 1). The data were not muted prior to stacking.

The image in Figure 7, with no static applied, could be considered as a standard result for Marmousi imaging. The sharp synclinal notch at approximately 5100 m in x and 500 m in depth is imaged as a broad synform, a feature that is quite common in the published
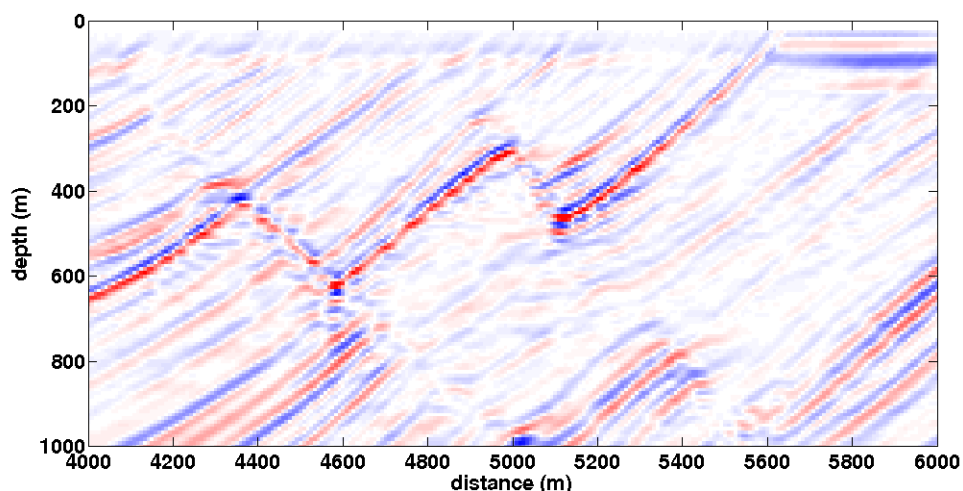

FIG. 11: Marmousi data; gap decon; whitened; -56 ms static; PSPI cross-correlation imaging.
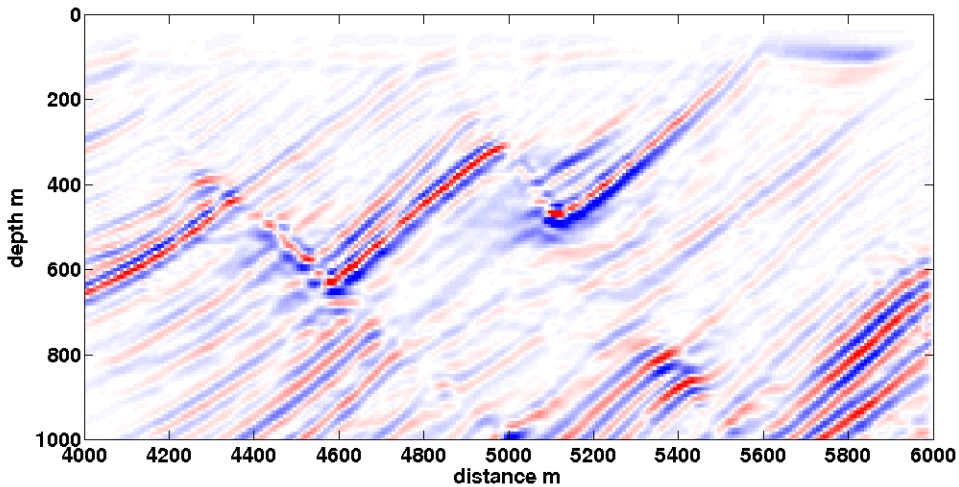
FIG. 12. Marmousi data; gap decon; whitened; -60ms static; Kirkpavg deconvolution imaging.

results (e.g. Shin et al. 2003, Kuehl and Sacchi 2003). In general, however, individual reflectors in the image are reasonably well focused, although there is significant mispositioning of both the left dipping reflectors and right dipping faults. For real data, the problem of uncorrected static shifts will probably become confused with velocity analysis. Further research is required on this subject.

The image in Figure 11 is produced using a static of −56 ms. The reference black sawtooth line is not plotted, as it exactly overlays the position of the strong red reflector. The image in Figure 12 is produced using a Kirchhoff average slowness extrapolator, a -60ms static, and a threshholding deconvolution imaging condition. The image is displaced downward 8 m to position the image reflectors at the spatial location of model reflectors. Some features of the deconvolution imaging condition image are superior to the 'optimal' image in Figure 11. Reflectors tend to be more continuous, although the deeper set of strong dipping reflectors between 5600 m and 6000 m in x appear to be less well resolved. More testing of the imaging conditions is required.

CONCLUSIONS

Prestack depth migration requires careful data preparation. This is true even for synthetic data sets such as the classic Marmousi acoustic data set. Ideally, the data should be preprocessed so that the embedded wavelet is zero-phase. A high dominant frequency and large bandwidth will produce a desirable zero-phase wavelet with a narrow peak width and small trough-height to peak-height ratio. Care is required when modelling the forward propagating source so as to produce a propagating zero-phase wavelet that has similar desirable characteristics. In general, a wavelet signature input as a single spatial impulse will not produce satisfactory results. Additional care is required when modelling the effect of source arrays and ghosting. I recommended use of the established method of seeding the source wavefield at a shallow depth using analytic constant-velocity Green's functions.

Even with optimal wavelet shaping, residual static shifts and phase rotations may remain, most likely in the processed data. A series of images produced using a subset of

the Marmousi data show that uncorrected static shifts result in positioning errors and, to a lesser extent, suboptimal focusing. If possible, the static shifts should be removed. For the Marmousi data set, a static shift and phase rotation were estimated using a simple finite difference model of an isolated reflector that included all the near-surface effects in the original Marmousi model. For real data, uncorrected static shifts will probably become confused with the velocity estimation. The choice of imaging conditions can also have a significant effect on the quality of the image. However, the results presented in this study at this point are inconclusive. Adaptive imaging conditions are a current research topic.

ACKNOWLEDGEMENTS

REFERENCES

Al-Saleh, S., and Geiger, H.D., 2004, Prestack constant velocity modelling and prestack depth migration using Hale's extrapolator, 2004 CREWES Research Report, **16**.

Bleistein, N., Cohen, J. K., and Stockwell, J. W., 2001, Mathematics of multidimensional seismic imaging, migration, and inversion, Springer-Verlag.

Brown, A.R., 1999: Interpretation of Three-Dimensional Seismic Data. AAPG Memoir 42.

de Bruin, C. G. M., Wapenaar, C. P. A., and Berkhout, A. J., 1990, Angle dependent reflectivity by means of prestack migration: Geophysics, Soc. of Expl. Geophys., **65**, 1223-1234.

Dellinger, J. A., Gray, S. H., Murphy, G. E. and Etgen, J. T., 2000, Efficient 2.5-D true-amplitude migration: Geophysics, Soc. of Expl. Geophys., **65**, 943-950.

Deregowski, S. M., and Brown, S. M., 1983, A theory of acoustic diffractors applied to Two-D models: Geophys. Prosp., Eur. Assn. Geosci. Eng., **31**, 293-333.

Gazdag, J., and Sguazzero, P., 1984, Migration of seismic data by phase shift plus interpolation: Geophysics, **49**, 124-131.

Geiger, H.D., 2001, Relative-amplitude-preserving prestack time migration by the equivalent offset method: PhD thesis, University of Calgary.

Geiger, H.D. and Daley, P.F., 2003, Finite difference modelling of the full acoustic wave equation in MATLAB: 2004 CREWES research report, University of Calgary.

Hanitzsch, C., 1997, Comparison of weights in prestack amplitude-preserving Kirchhoff depth migration: Geophysics, Soc. of Expl. Geophys., **62**, 1812-1816.

Kelly, S., and Ren, J., 2003, Key elements in the recovery of relative amplitudes for prestack, shot record migration, 73rd Ann. Internat. Mtg.: Soc. of Expl. Geophys., 1110-1113.

Kuehl, H., and Sacchi, M., 2003, Least-squares wave-equation migration for AVP/AVA inversion: Geophysics, Soc. of Expl. Geophys., **68**, 262-273.

Ricker, N., 1953, Wavelet contraction wavelet expansion and the control of seismic resolution: Geophysics, Soc. of Expl. Geophys., **18**, 769-792.

Sava, P. C., and Fomel, S., 2003, Angle-domain common-image gathers by wavefield continuation methods: Geophysics, Soc. of Expl. Geophys., **68**, 1065-1074.

Shin, C., Ko, S., Kim, W., Min, D. -J., Yang, D., Marfurt, K., Shin, S., Yoon, K. and Yoon, C. H., 2003, Traveltime calculations from frequency-domain downward-continuation algorithms: Geophysics, Soc. of Expl. Geophys., **68**, 1380-1388.

Valenciano, A.,. and Biondi, B., 2003, 2D deconvolution imaging condition for shot profile migration, 73rd Ann. Internat. Mtg.: Soc. of Expl. Geophys., 1059-1062.

Versteeg, R., and Grau, G., Eds., 1991, The Marmousi experience: Proc. 1990 Eur. Assn. Expl. Geophys. Workshop.

Wapenaar, K., 1998, Reciprocity properties of one-way propagators: Short Note: Geophysics, Soc. of Expl. Geophys., **63**, 1795-1798.

Yilmaz, O., 2001, Seismic Data Analysis. SEG Investigations in Geophysics 10.

Zhu, J., and Lines, L., 1998, Comparison of Kirchhoff and reverse-time migration methods with applications to prestack depth imaging of complex structures: Geophysics, Soc. of Expl. Geophys., **63**, 1166-1176.